


Article

Experimental Study on the Characteristics of Corrosion-Induced Cracks and Steel Corrosion Depth of Carbonated Recycled Aggregate Concrete Beams

Pengfei Gao ¹, Jian Wang ^{2,*} , Bo Chen ³, Mingxin Bai ⁴ and Yuanyuan Song ³

¹ Inspection and Certification Co., Ltd. MCC, Beijing 100088, China; gaopengfei@cribc.com

² School of Civil Engineering, Sun Yat-sen University, Guangzhou 510275, China

³ School of Civil Engineering, Beijing Jiaotong University, Beijing 100044, China; 21121020@bjtu.edu.cn (B.C.); yysong@bjtu.edu.cn (Y.S.)

⁴ Shenzhen China Nuclear Power Engineering Design Co., Ltd., Shenzhen 518116, China; baimingxin@cgnpc.com.cn

* Correspondence: wangj833@mail.sysu.edu.cn

Abstract: The durability of carbonated recycled aggregate concrete (C-RAC) beams is still unclear at present. In this paper, the characteristics of corrosion-induced cracks and the steel corrosion depth of C-RAC beams were investigated through the accelerated corrosion test. The results showed that when accelerating corrosion to the 40th day, compared to the non-carbonated recycled aggregate concrete (NC-RAC) beam, the corrosion-induced cracking area of the C-RAC beam with a 100% carbonated recycled coarse aggregate (C-RCA) replacement ratio decreased by 40.00%, while the total length of the corrosion-induced cracks (CCs) increased by 51.82%. The type of probability distribution for the width of the CCs on the tension side of the C-RAC beams was a lognormal distribution. Compared with the NC-RAC beam, the mean value of the width of the CCs of the C-RAC beam with a 100% C-RCA replacement ratio decreased by 66.67%, the crack width distribution was more concentrated, and the quartiles and median were all reduced. With an increase in the C-RCA replacement ratio, the fractal dimension and the scale coefficient of CCs on the tension side of the beams showed an approximate trend of first increasing and then decreasing. The distribution of the corrosion depth of longitudinal tensile steel bars in the C-RAC beams was a mainly normal distribution. When the C-RCA replacement ratio increased from 30% to 100%, the mean value of the corrosion depth of the longitudinal tensile steel bars decreased by 33.46%, and the trend of changes in the quartiles and medians was basically the same as the trend of changes in the mean value. The research results can provide some reference for promoting the engineering application of C-RAC beams.

Keywords: carbonated recycled aggregate concrete beams; corrosion-induced cracks; fractal characteristics; corrosion depth; probability distribution



Citation: Gao, P.; Wang, J.; Chen, B.; Bai, M.; Song, Y. Experimental Study on the Characteristics of Corrosion-Induced Cracks and Steel Corrosion Depth of Carbonated Recycled Aggregate Concrete Beams. *Buildings* **2024**, *14*, 3889. <https://doi.org/10.3390/buildings14123889>

Academic Editor: Oldrich Sucharda

Received: 11 November 2024

Revised: 29 November 2024

Accepted: 2 December 2024

Published: 4 December 2024



Copyright: © 2024 by the authors. Licensee MDPI, Basel, Switzerland. This article is an open access article distributed under the terms and conditions of the Creative Commons Attribution (CC BY) license (<https://creativecommons.org/licenses/by/4.0/>).

1. Introduction

With the rapid development of urbanization in China, a large amount of waste concrete is generated and randomly piled up, which not only affects the beauty of the urban environment and wastes land resources but also pollutes the environment and poses a potential threat to the lives of people. From the perspective of environmental protection and solid waste utilization, it is imperative to recycle and reuse the waste concrete. In general, the waste concrete is often crushed into recycled aggregates with a certain particle size, which are used to replace natural aggregates and mix with cementitious materials, water, and so on to obtain recycled aggregate concrete (RAC) [1,2]. In 2019, a RAC office building with a recycled coarse aggregate (RCA) replacement ratio of 30% was put into use in the Lintong green industrial park in Shaanxi province, which truly achieves the goal of “producing–utilizing–abandoning–reproducing–reusing” concrete. Therefore, RAC is an

important direction for achieving the reuse of waste concrete, which is of great significance for environmental protection, resource conservation, and low-carbon circular development.

Compared to the natural aggregates such as sand and crushed stone, the recycled aggregates have a layer of old mortar attached, resulting in more initial defects, which have higher water absorption, porosity, and lower strength. Especially, when adding recycled aggregates to concrete, various interfacial transition zones (ITZs) are formed, leading to more internal defects in RAC [3,4]. Therefore, compared with natural aggregate concrete (NAC), RAC has poorer mechanical properties and durability [5–7]. In order to solve a series of problems caused by recycled aggregates, some researchers have conducted research on the strengthening of recycled aggregates and proposed different methods for recycled aggregates to remove the old mortar and improve the ITZs, including mechanical grinding, soaking in acid solution or volcanic ash slurry, microorganism modification, and so on [8]. However, these strengthening methods for recycled aggregates also have certain limitations, including high requirements for mechanical equipment, material waste, environmental pollution, and poor economic efficiency.

The carbonation strengthening of recycled aggregates is one of the highlights in the research field of RAC in recent years [9]. The old mortar on the surface of recycled aggregates contains a lot of alkaline components, of which calcium hydroxide accounts for about 20–25% of the volume of hydration products, and calcium silicate hydrate gel accounts for about 50–60% [10]. The utilization of a greenhouse gas, namely CO₂, to modify recycled aggregates is an effective, economical, and environmentally friendly method [11–15]. On the one hand, the carbonation products (i.e., calcium carbonate, silica gel, etc.) can be used to fill the micro-cracks and micro-pores in the recycled aggregates, thereby reducing the porosity of recycled aggregates, compacting the ITZs, and improving the mechanical properties and durability of RAC. On the other hand, the carbonation treatment of 1000 kg of RCA can absorb 7.9–11 kg CO₂ [11], which can reduce the concentration of CO₂ in the atmosphere, with good economic and environmental benefits.

The concrete mixed with carbonated RCA (C-RCA) is called carbonated recycled aggregate concrete (C-RAC), while the concrete prepared with non-carbonated RCA (NC-RCA) is called non-carbonated recycled aggregate concrete (NC-RAC). After the carbonation of RCA, the compressive strength of RAC can be significantly enhanced. Wang [14] indicated that compared with the NC-RAC, the compressive strengths of C-RAC at 28 and 90 days increased by 13.1% and 14.2%, respectively. Cao [15] found that, when the RCA replacement ratio was 100%, the compressive strengths of C-RAC and NC-RAC at 28 days were reduced by 4% and 16.3% compared to NAC, showing a significant increase in the compressive strength of C-RAC. Kou et al. [16] revealed that the compressive strength of C-RAC at 28 days was only 1% to 3% lower than that of NAC, while the compressive strength of NC-RAC was 8% to 10% lower than that of NAC. Lu et al. [10] confirmed that, compared with NC-RAC, the compressive strengths of C-RAC with a 100% C-RCA replacement ratio at 7 and 28 days increased by 11.7% and 14.2%, respectively. Lin [17] poured RAC mixed with C-RCA, and the results showed an increase of 15.3% and 16.2% in the prism compressive strength and cubic compressive strength at 28 days, respectively.

The carbonation treatment of RCA obviously improves the resistance to chloride ion penetration of RAC. Wang [14] found that the chloride diffusion coefficients of C-RAC and NC-RAC were about 1.06 and 1.6 times those of NAC; that is, compared with NC-RAC, the resistance to chloride ion penetration of C-RAC significantly improved. Kou et al. [16] showed that the resistance to chloride ion penetration of C-RAC increased by 41% to 46% at 28 days. Wang [18] discovered that the chloride diffusion coefficient of C-RAC was 3.1–15.3% lower than that of NC-RAC, indicating an improved resistance to chloride ion penetration of C-RAC. Huang et al. [19] pointed out that the resistance to chloride ion penetration of C-RAC was 5.1–22.1% higher than that of NC-RAC. Xuan et al. [20] compared the resistance to chloride ion penetration of C-RAC with that of NC-RAC and found that the former was 36.4% higher than the latter.

The carbonation of RCA is beneficial for improving the corrosion resistance of steel bars in RAC. In corrosive environments, the corrosion probability of steel bars in C-RAC was significantly reduced compared to NC-RAC [21,22], which is mainly due to the fact that the carbonation treatment of RCA improves the ITZs of C-RAC, reduces the internal defects of C-RAC, and thus reduces the diffusion channels for corrosive ions inside C-RAC. Liang et al. [21] noted that after the carbonation of RCA, the corrosion current density and corrosion potential of steel bars in RAC decreased by 33% and 16%, respectively. Zheng et al. [23] showed that, when the RCA replacement ratio was 50%, the corrosion current density of steel bars after 28 days of electrification corrosion in RAC with different carbonation times (i.e., 12 h, 24 h, and 48 h) of RCA was 15.8%, 28.4%, and 30.5% lower than that of NC-RAC, while when the RCA replacement ratio was 100%, the corrosion current density of steel bars in C-RAC was reduced by 17.4%, 35.8%, and 35.9%, respectively. Liu [24] pointed out that when using CO₂ to strengthen RCA, the corrosion rates of stirrups and longitudinal steel bars in large eccentric RAC columns decreased by 14.7% and 11.2%, respectively.

In summary, the carbonation strengthening of recycled aggregates has a positive impact on the strength, the resistance to chloride ion penetration, and the resistance to steel corrosion of RAC. However, the above research mainly focused on the durability of C-RAC at the level of materials, which makes it challenging to accurately understand and predict the durability of C-RAC members. At present, some researchers have studied the corrosion of steel bars and the flexural performance of the NC-RAC beams in corrosive environments [25–30]. However, the durability of C-RAC beams in the corrosive environments is still unclear, and the characteristics of corrosion-induced cracks and the corrosion depth laws of steel bars in the C-RAC beams need to be explored. In order to promote the engineering application of RAC and improve the durability of RAC beams, in this study, the distribution and development laws of corrosion-induced cracks (CCs) as well as the corrosion depth characteristics of steel bars in C-RAC beams were studied through the accelerated corrosion test.

2. Experimental Program

2.1. Materials

The cementitious material used was ordinary Portland cement with a strength of 42.5 MPa, and tap water was used for mixing water. Natural river sands with a fineness modulus of 2.7 were adopted as the fine aggregates. The coarse aggregates included natural coarse aggregates (NCAs), C-RCA, and NC-RCA, among which NCA was macadam with a particle size of 5–20 mm. According to the Chinese Standard GB/T 25177 [31], the waste concrete with a strength grade of C30 was crushed into aggregates, and then the aggregates were cleaned, sieved, and classified to obtain the required RCA with a particle size of 5–20 mm. Some of the prepared RCA was placed into a carbonation chamber for carbonation strengthening, while the rest accepted no special treatment. According to the Chinese Standard GB/T 50082 [32], the concentration of CO₂, relative humidity, and carbonation temperature in the carbonation chamber were set to (20 ± 3)%, (70 ± 5)%, and (20 ± 2)°C, respectively. After 7 days of carbonation, the RCA was sprayed with 1% phenolphthalein alcohol solution, and there was no color change on the surface of the RCA, indicating the approximately complete carbonation of the RCA. The microscopic morphologies of the NC-RCA and C-RCA were observed by using a scanning electron microscope (SEM), the basic properties of coarse aggregates are tabulated in Table 1, and the mix proportions of different types of concrete are all listed in Table 2. The specimens of NC-RAC and C-RAC are depicted in Figure 1. The compressive strength of NC-RAC with an NC-RCA replacement ratio of 100% at 28 days is 36.4 MPa, and the compressive strengths of C-RAC with C-RCA replacement ratios of 30%, 50%, 75%, and 100% at 28 days are 39.1, 39.4, 41.0, and 42.5 MPa, respectively.

Table 1. Basic properties of coarse aggregates.

Type	Apparent Density (kg/m ³)	Adhesion Rate of Mortar (%)	Crushing Index (%)	Absorption Rate of Water (%)
NCA	2675	/	4.73	0.22
NC-RCA	2525	28.5	14.44	3.85
C-RCA	2605	30.5	10.52	3.13

Table 2. Mix proportions of concrete.

Water-Cement Ratio	RCA Replacement Ratio (%)	Materials (kg/m ³)						Water-Reducing Admixture (%)
		Cement	Sand	NCA	NC-RCA	C-RCA	Water	
0.5	100			0	1116	0		2
	30			781	0	335		
	50	400	684	558	0	558	200	
	75			279	0	837		
	100			0	0	1116		

**Figure 1.** NC-RAC and C-RAC specimens.

2.2. Design of Beams

Considering a combination of RCA types (i.e., NCA, NC-RCA, and C-RCA) and RCA replacement ratios (i.e., 30%, 50%, 75%, and 100%), a total of 5 beams were designed for testing. The parameters of the designed beams are listed in Table 3. All beams were divided into two groups based on the RCA types, and the beam NC-RAC-100 was regarded as the control group. The second group (i.e., labelled C-RAC-30, C-RAC-50, C-RAC-75, and C-RAC-100) were beams made of C-RAC. The dimensions and reinforcement layout of the beams are displayed in Figure 2. All the steel bars in the beams were ribbed steel bars, whose diameters were 8 mm and 12 mm, respectively. The yield and ultimate strengths of the steel bars with a diameter of 8 mm were 506.7 MPa and 616.7 MPa, respectively. The yield and ultimate strengths of the steel bars with a diameter of 12 mm were 451.7 MPa and 625.0 MPa, respectively.

Table 3. Parameters of the designed beams.

Beam ID	Coarse Aggregate	Replacement Ratio (%)	Corrosion Duration (Days)
NC-RAC-100	NC-RCA	100	40
C-RAC-30	C-RCA	30	40
C-RAC-50		50	40
C-RAC-75		75	40
C-RAC-100		100	40

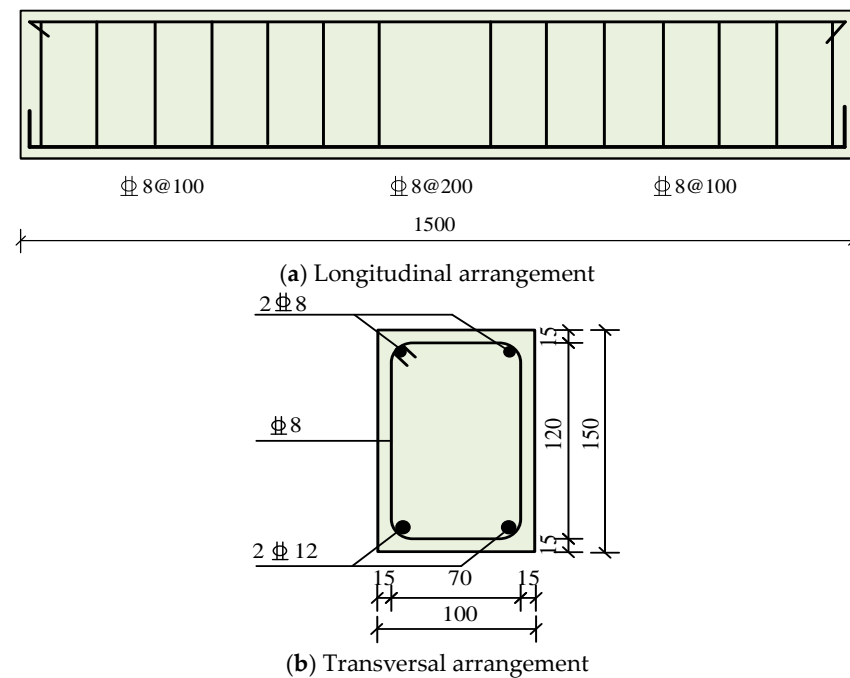


Figure 2. Details of the beams (unit: mm).

Before tying the skeletons of steel bars, the rust on the surface of the steel bars was wiped and cleaned, and then the treated steel bars were weighed by an electronic scale with an accuracy of 0.01 g for the following calculation of the mass loss. Subsequently, the steel skeletons were bound with iron wire as shown in Figure 3.



Figure 3. Steel skeletons of the beams.

Before pouring concrete, one end of the wire was fixed with insulation tape on each longitudinal tensile steel bar in the beams as depicted in Figure 4, and the other end was led out to prepare for the subsequent accelerated corrosion test. After 48 h of curing, all beams were demolded, and then they were cured for 28 days.

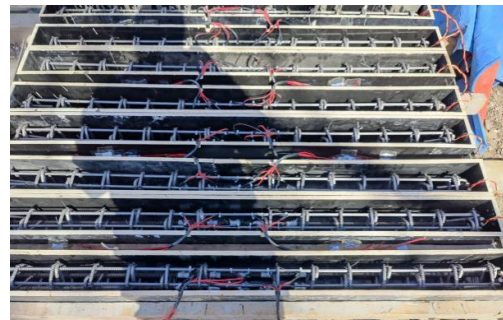
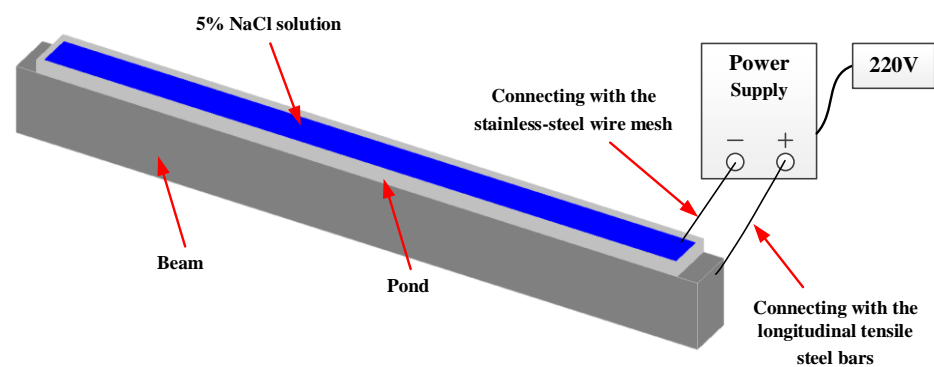


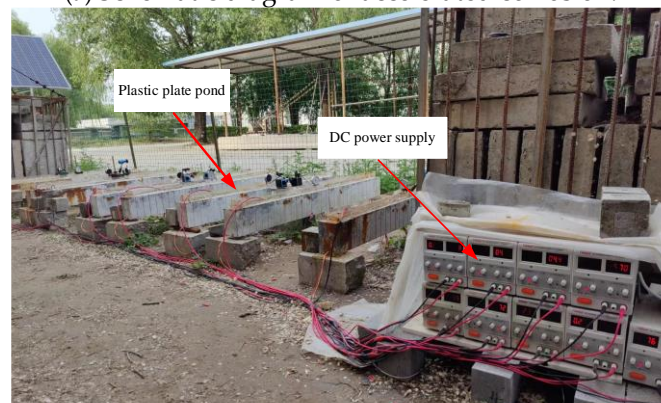
Figure 4. Connecting the wire and the steel bars.

2.3. Accelerated Corrosion Test

As illustrated in Figure 5, the beams were placed on the test field, a small pond made of plastic plates was 1400 mm in length, 90 mm in width, and 100 mm in height, and an electrolytic cell was set in the middle above each beam, and then a 5% NaCl solution was poured into the small pond with a liquid level of 20 to 30 mm. During the process of electrochemical corrosion, a power supply was adopted, with an output current of 0–5 A and an output voltage of 0–30 V. The positive pole of the power supply was connected to the longitudinal tensile steel bars of the beams, while the negative pole of the power supply was connected to a stainless-steel wire mesh in the plastic-plate pond, which served as an auxiliary electrode. After turning on the power, a closed circuit was formed.



(a) Schematic diagram of accelerated corrosion.



(b) Physical photo of accelerated corrosion.

Figure 5. Accelerated corrosion test of the beams.

Some researchers found that, when the current density was less than $200 \mu\text{A}/\text{cm}^2$, the characteristics of the electrification corrosion of steel bars in concrete were similar to those of the corrosion of steel bars in the actual situations [33–35]. Thus, the current density was maintained at $200 \mu\text{A}/\text{cm}^2$ in this corrosion test, and for the purpose of the constant current density, the constant current and variable voltage mode of the power supply was adopted during the corrosion test. The theoretical corrosion rate (i.e., mass loss) of longitudinal tensile steel bars in the beams was designed as 9%, according to Faraday's law; the estimated corrosion duration for each beam was 40 days.

For the convenience of collecting the characteristics of CCs, after finishing the standard curing, the squares with a side length of 50 mm were drawn on the surface of the beams by using a marker pen. During the accelerated corrosion test, the 5% NaCl solution in the electrolytic cell was regularly replaced, and the rust products were also cleaned up. The distributions of the CCs on the tension side of the RAC beams at the corrosion durations of 8, 20, 30, and 40 days were collected and recorded, respectively. When recording the

CCs, a tracing paper was tightly attached to the surface of the beams, and then the CCs were proportionally depicted on it. Moreover, the width of the CCs was measured every 50 mm by using a crack width visualizer with an accuracy of 0.02 mm and recorded in the corresponding positions.

2.4. Measurement of the Mass Loss and Corrosion Depth of Steel Bars

After the accelerated corrosion test, a bending failure test was carried out on each corroded beam. After the bending failure test, all corroded beams were broken, and the corroded steel bars were exposed as shown in Figure 6. It was evident that the steel bars were corroded, with reddish brown rust products adhering to the surface of the surrounding concrete and the steel bars. According to the Chinese Standard GB/T 50082 [32], the concrete adhering to the surface of corroded steel bars was scraped off with a rasp knife, and then the steel bars were pickled with 12% hydrochloric acid. After removing the rust from the steel bar surface, the steel bar was cleaned with potable water and then neutralized with saturated lime water and finally rinsed again with potable water. In order to calibrate the mass loss measurement of corroded steel bars, two uncorroded steel bars of the same type and size were also pickled with 12% hydrochloric acid when pickling the corroded steel bars. After the steel bars were dried, the mass of each steel bar was weighed by an electronic scale with an accuracy of 0.01 g. The mass loss of each steel bar was calculated by Equation (1). In order to study the distribution characteristics of the corrosion depth of longitudinal tensile steel bars along their length direction in different beams, the remaining diameters of the longitudinal tensile steel bars were measured with a vernier caliper at an interval of 8 mm.

$$\eta = \frac{m_s - m_c}{m_s} \times 100\% \quad (1)$$

where η is the mass loss of a steel bar (%); m_s is the mass of a steel bar before corrosion (g); and m_c is the mass of a steel bar after corrosion (g).



Figure 6. Corrosion of steel bars.

3. Results and Discussion

3.1. Deterministic Analysis of CCs of the C-RAC Beams

The distributions of CCs of each beam at 8, 20, 30, and 40 days are shown in Figures 7–10. During the recording process, the extended or newly added CCs at 8, 20, 30, and 40 days are plotted in black, red, green, and blue, respectively. Due to the late appearance, small width, and slow development of CCs on both sides of the beams, they are only collected once on the 40th day of the accelerated corrosion test as illustrated in Figure 10.

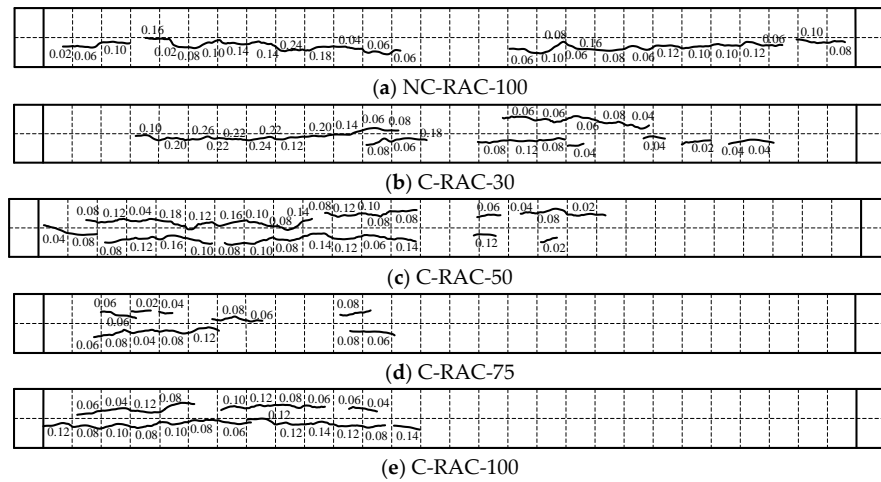


Figure 7. Distribution of the CCs on the tension side of the beams on the 8th day of accelerated corrosion (unit: mm).

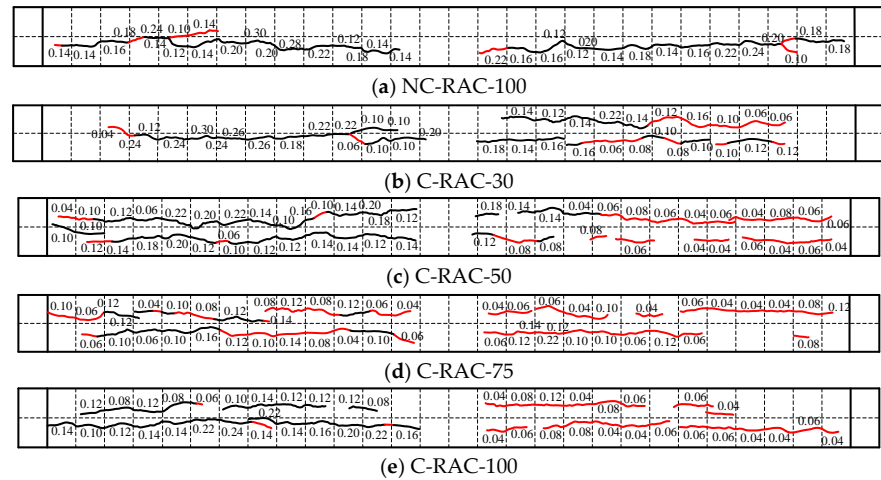


Figure 8. Distribution of the CCs on the tension side of the beams on the 20th day of accelerated corrosion (unit: mm).

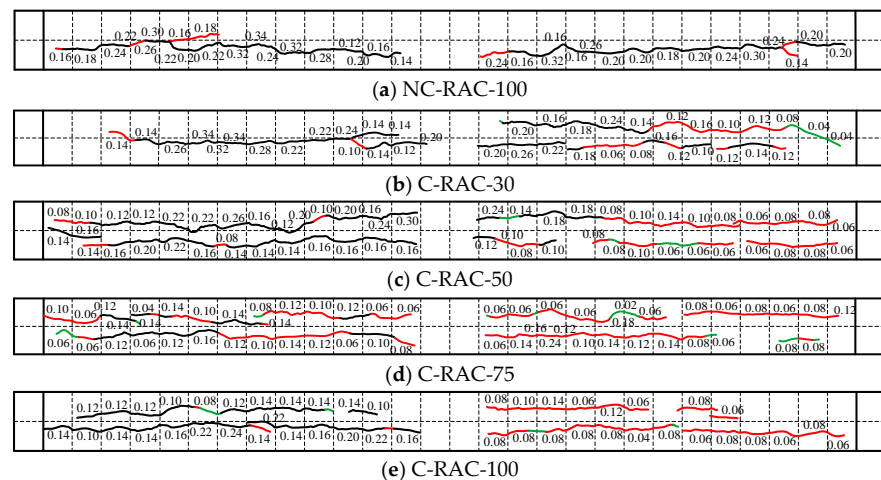


Figure 9. Distribution of the CCs on the tension side of the beams on the 30th day of accelerated corrosion (unit: mm).

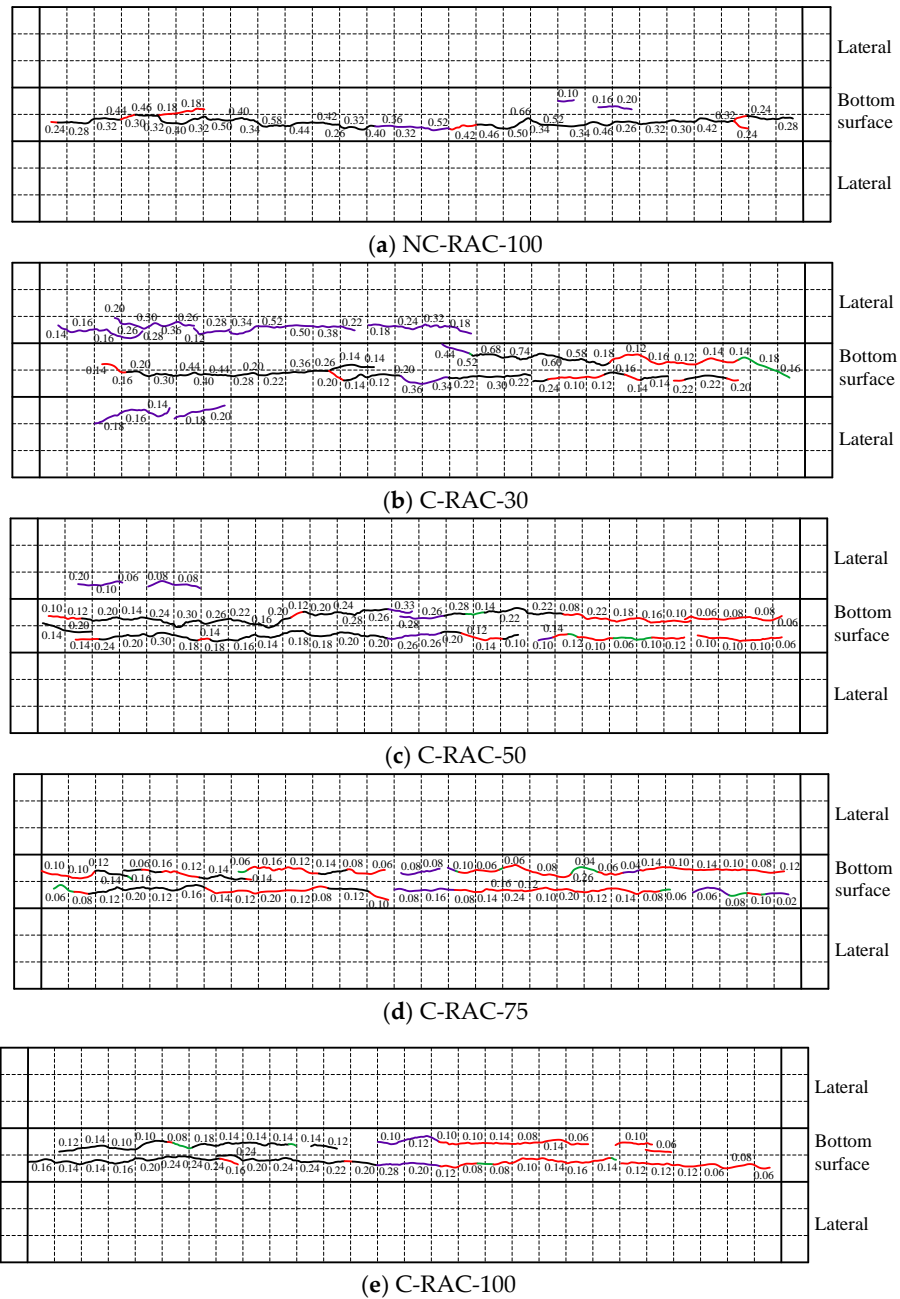


Figure 10. Distribution of the CCs on the tension side of the beams on the 40th day of accelerated corrosion (unit: mm).

When the accelerated corrosion test lasts for 3–4 days, the initial CCs are found on the tension side of the beams, mainly concentrated in the area of the small pond. As the corrosion time increased, the small CCs continue to extend and gradually connects together, forming two main longitudinal cracks roughly parallel to the longitudinal tensile steel bars, and the width of the CCs also increases. During the process of the accelerated corrosion test, no transverse CCs caused by the stirrups are observed, which may be due to the small diameter of the stirrups and the insufficient corrosion force generated in the early stage of corrosion, making it difficult to cause cracking of the concrete cover. The corrosion-induced cracking on the tension side of the beams is severe, while the length and width of the CCs on the lateral sides are both small. The main reason for this is that the small pond is only arranged on the tension side of the beams, resulting in more substances such as chloride ions and water around the longitudinal tensile steel bars near the small pond side than that on the lateral sides. Therefore, only the CCs on the

tension side of the beams are discussed in this section. The distributions of CCs at 8, 20, 30, and 40 days are input into CAD, and the length of the CCs is statistically calculated based on the spline characteristics in CAD. The areas of the CCs are approximately determined based on the length and width of the CCs in each grid, and the results of the area and total length of the CCs are shown in Figures 11 and 12.

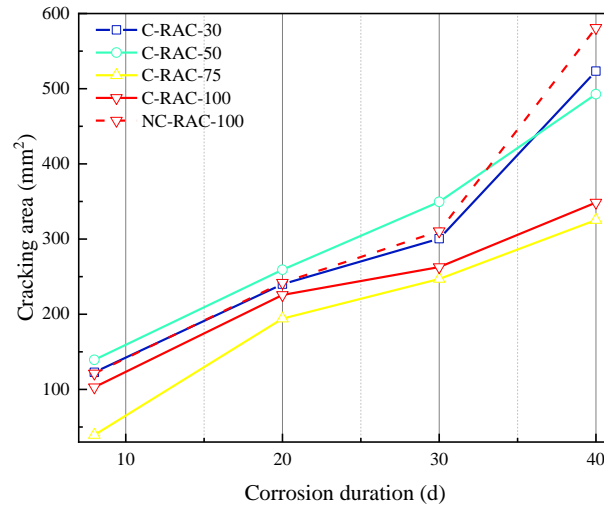


Figure 11. Cracking area on the tension side of the beams.

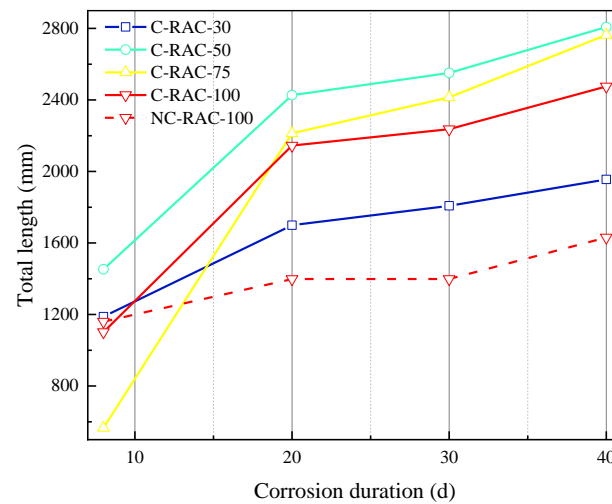


Figure 12. Total length of CCs on the tension side of the beams.

As shown in Figures 11 and 12, with the increase in the C-RCA replacement ratio, there is no obvious rules for the size of the cracking area and the total length of CCs of C-RAC beams. The reason may be that compared to natural aggregates, RCA is characterized by its significant differences in physical and chemical properties, and the alkalinity of RCA decreases during carbonation, bringing significant uncertainty to the overall performance and corrosion-induced behavior of concrete. In addition, different C-RCA replacement ratios may cause changes in the distribution of internal stress of the beams, which results in different cracking propagation paths, leading to an irregular total length of CCs and the cracking area. When the accelerating corrosion reaches the 8th, 20th, 30th, and 40th day, the corrosion-induced cracking area of the C-RAC-100 beam decreases by 15.18%, 6.78%, 15.36%, and 40.00%, respectively, compared to that of the NC-RAC-100 beam. The reason is that the calcium carbonate and other substances are generated by the carbonation strengthening treatment of the RCA, which fills the pores and micro-cracks inside the aggregates to make the RCA denser, as shown in Figure 13. Moreover, the bonding strength

between the aggregates and the cement paste is improved, which reduces the porosity and pore connectivity in the ITZs [36], and as a result, the RAC's resistance to chloride ion penetration is improved, and the corrosion degree of the steel bars in the C-RAC beams decreases. On the 8th day of accelerated corrosion, the total length of the CCs on the C-RAC-100 beam is 4.99% less than that on the NC-RAC-100 beam. However, at the 20th, 30th, and 40th day of accelerated corrosion, compared to the NC-RAC-100 beam, the total length of the CCs on the C-RAC-100 beam increases by 53.37%, 59.91% and 51.82%, respectively. The reason is that the corrosion-induced cracking degree of concrete cover can be effectively reduced by carbonating RCA, making the C-RAC beams less prone to crack during the early stage of accelerated corrosion, which lead to a smaller total length of the CCs compared to the NC-RAC-100 beam. However, due to the C-RAC having fewer internal defects than the NC-RAC, the C-RAC is prone to producing some evenly distributed small cracks, while the NC-RAC is prone to producing a small number of large cracks along the defects under the same action of the rust expansion force. As the corrosion time increases, the rust expansion force increases, various small cracks may connect together, and longer through cracks are formed, leading to a greater total length of the CCs of the C-RAC-100 beam in the later stage of accelerated corrosion compared to that of the NC-RAC-100 beam. However, due to the carbonation strengthening treatment of RAC, the corrosion-induced cracking degree of the concrete cover can be effectively reduced. Even if some small cracks occur, they are still not enough to offset the positive effects of the carbonation strengthening treatment. Therefore, compared to the NC-RAC-100 beam, the width of the CCs of the C-RAC beams is smaller, and the overall area of CCs is significantly smaller.

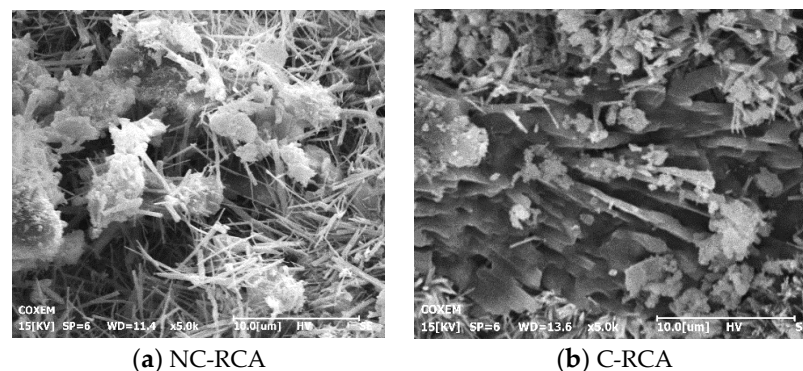


Figure 13. Comparison of the microscopic morphologies between NC-RCA and C-RCA.

3.2. Probability Analysis of the Width of the CCs of the C-RAC Beams

The interior of the C-RAC beams is uneven, and the physical and chemical properties of the C-RCA are significantly different from those of the NCA. Therefore, the width of the CCs along the length direction of the C-RAC beams has a large degree of randomness, and the test results have a certain degree of uncertainty and variability. The probability analysis method considers various uncertainties and variability to make the analysis results more comprehensive and reliable. Based on the data of the width of CCs at 40 days, a probability analysis method is used to analyze the width of CCs. The frequency distribution histograms for the width of CCs of the beams are drawn in Figure 14. According to the research results of some researchers, the width of CCs mainly followed a normal distribution, a lognormal distribution, or an exponential distribution [1]. Therefore, in the software Origin 2018, the curve fitting on the frequency distribution histograms are performed by using the above three types of distributions. The best curve fitting is shown in Figure 14 and the fitted values of the probability distribution parameters are listed in Table 4. The probability

density functions of the normal distribution and the lognormal distribution are shown in Equations (2) and (3), respectively.

$$y = y_0 + A \exp \left[-\frac{(x - x_c)^2}{2w^2} \right] \quad (2)$$

$$y = y_0 + \frac{A}{\sqrt{2\pi}wx} \exp \left[-\frac{[\ln(x/x_c)]^2}{2w^2} \right] \quad (3)$$

where y_0 , x_c , w , and A are all unknown parameters; and x is an independent variable.

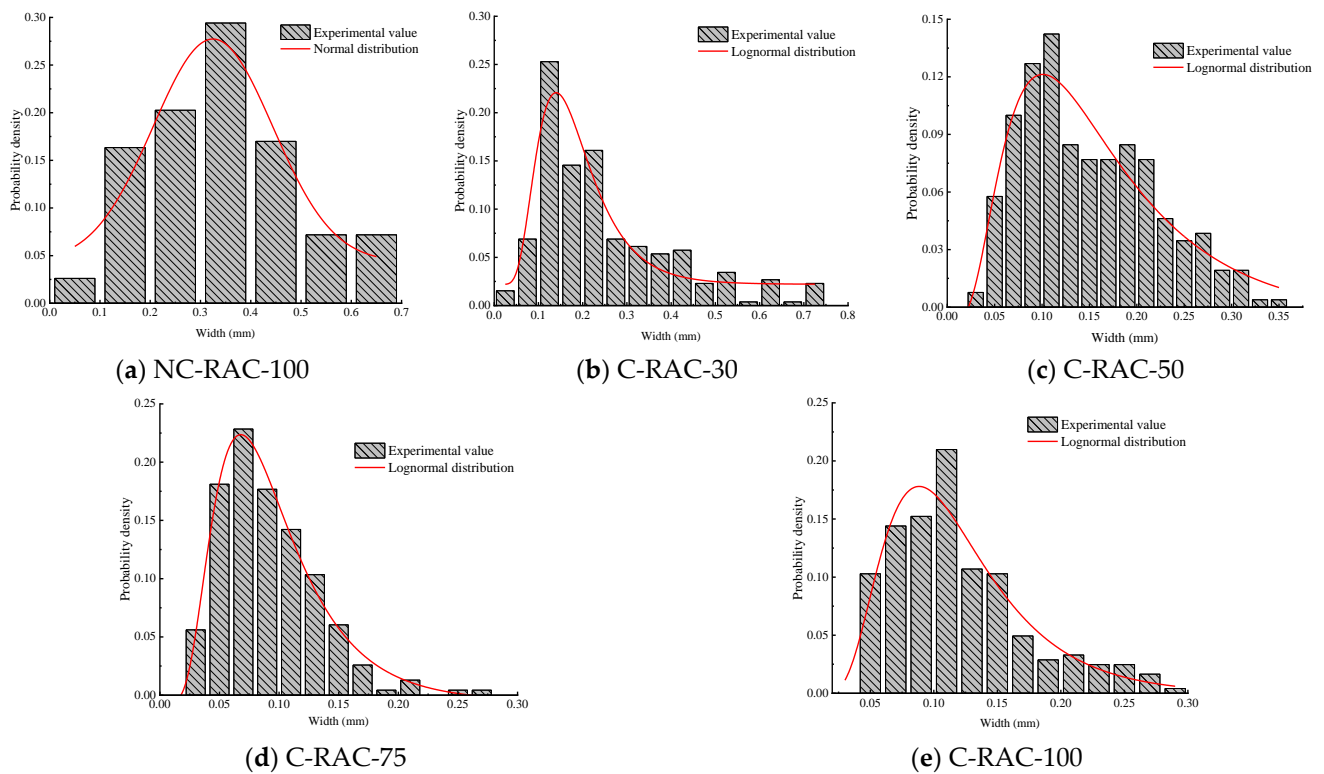


Figure 14. Frequency distribution histograms of the width of CCs of the beams.

Table 4. Fitted values of probability distribution parameters of the width of CCs.

Beam ID	Distribution Function	y_0	x_c	w	A	R^2
NC-RAC-100	Normal	0.043	0.325	0.119	0.234	0.902
C-RAC-30	Lognormal	0.022	0.169	0.436	0.033	0.886
C-RAC-50	Lognormal	−0.007	0.148	0.619	0.024	0.916
C-RAC-75	Lognormal	−0.006	0.067	0.494	0.022	0.990
C-RAC-100	Lognormal	−0.001	0.110	0.465	0.021	0.908

From Figure 14, it is clear that the type of probability distribution of the width of CCs on the tension side of the C-RAC beams is a lognormal distribution, with the width of CCs of the NC-RAC-100 beam following a normal distribution. According to the mean value ($E(X)$) and variance ($D(X)$) of the width of CCs, the coefficient of variation (C_v) can be obtained:

$$C_v = \frac{\sqrt{D(X)}}{E(X)} \quad (4)$$

As depicted in Figure 15, with the increase in the C-RCA replacement ratio, the mean value of the width of CCs shows a decreasing trend. As the C-RCA replacement ratio increases from 30% to 100%, the mean value of the width of CCs decreases by 54.17%. After carbonation of RCA, the mean value of the width of CCs decreases, and the mean value of the width of CCs of the C-RAC-100 beam reduces by 66.67% compared to that of the NC-RAC-100 beam. This is because a dense carbonation layer is formed on the surface of the RCA during the carbonation process, reducing the permeability of C-RAC, which not only reduces the corrosion rate of steel bars, but also makes the C-RAC exhibit better stability when subjected to corrosion-induced pressure. Overall, the corrosion-induced cracking degree of the concrete cover is reduced by the carbonation of RCA, lowering the mean value of the width of CCs of C-RAC beams.

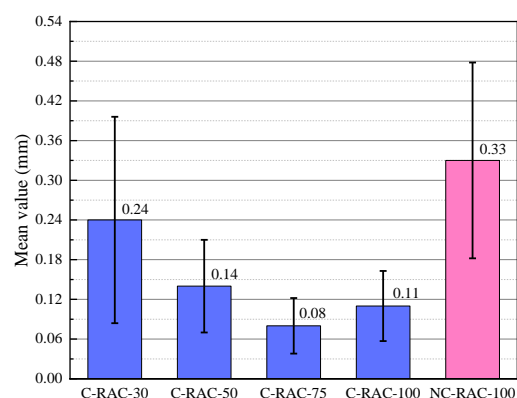


Figure 15. Mean value of the width of CCs.

The C_v can reflect the dispersion degree of the width of CCs around its mean value. Figure 16 shows that, with the increase in the C-RCA replacement ratio, the C_v shows a decreasing trend, namely the dispersion degree of the width of CCs around its mean value is reduced. When the C-RCA replacement ratio increases from 30% to 100%, the C_v of the width of CCs of the C-RAC beams decreases by 23.47%, and that of the C-RAC-100 beam increases by 7.95% compared to that of the NC-RAC-100 beam.

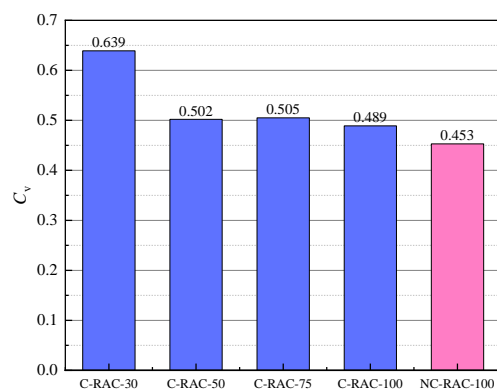


Figure 16. C_v of the width of CCs.

The statistical distribution characteristics of the width of CCs can be described by a box plot, as shown in Figure 17. It can be seen from Figure 17 that when the C-RCA replacement ratio increases from 30% to 100%, the size of the box plot shows a decreasing trend; that is, the crack width tends to be concentrated, and the trend of changes in quartiles and medians is basically the same as the trend of changes in the mean value. Compared with the NC-RAC-100 beam, the crack width distribution of the C-RAC-100 beam is more concentrated, and the mean value, quartiles, and median are all reduced.

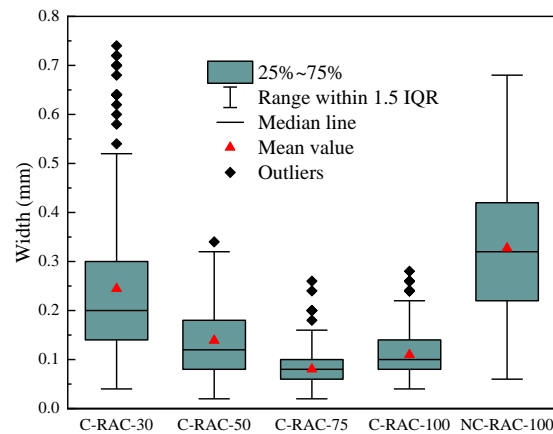


Figure 17. Box plot of the width of CCs.

3.3. Fractal Characteristics Analysis of CCs of the C-RAC Beams

The analysis of the cracks of concrete structures mainly focuses on the length, width, and quantity. In most cases, the geometric shape, distribution, and extension characteristics of cracks can only be vaguely described by using words such as sparse and dense, which cannot be quantitatively analyzed. Some studies confirmed that the stress cracks [37,38] and CCs [39] met self-similarity in probability theory and statistics, which could be quantitatively analyzed through fractal theory. At present, the box counting method is mainly adopted for calculating the fractal dimension [40,41]. Firstly, a series of boxes with the characteristic size (r_i) are determined, and the minimum number of boxes required to cover the fractal object ($N(r_i)$) is counted. Then, the natural logarithm of r_i and $N(r_i)$ is calculated. If both values obtained satisfy Equation (5), which indicates that the shape of the fractal object satisfies the self-similarity criteria, the fractal theory can be used for research.

$$\ln N(r) = -D \ln r + \ln C \quad (5)$$

where D is the fractal dimension; and C is the scale coefficient.

The box counting method is adopted in this section to determine the fractal dimension of CCs on the tension side of each beam during the accelerated corrosion test, with an r_i of 100 mm, 50 mm, 20 mm, 10 mm, and 5 mm. The relationship between r_i and $N(r_i)$ is shown in Figure 18, and the computed results are presented in Table 5.

It can be seen from Figure 18 and Table 5 that there is a clear linear relationship between $\ln N(r_i)$ and $\ln r_i$, demonstrating that the CCs on the tension side of both NC-RAC and C-RAC beams has obvious fractal characteristics and can be analyzed by using fractal theory. As depicted in Figure 19, with an increase in the C-RCA replacement ratio, the fractal dimension of CCs on the tension side of the beams shows an approximate trend of first increasing and then decreasing. After 8 days of accelerated corrosion, the lengths of CCs on the tension side of the NC-RAC and C-RAC beams are small, and the self-similarity displayed is not apparent, and as a result, the fractal dimension is small. With the continuous generation and extension of CCs, the fractal dimension of the CCs continuously goes up, with enhanced self-similarity. In the late period of the accelerated corrosion test, the length of CCs always grows slowly; hence, the curves of the fractal dimension are relatively flat. In comparison between the C-RAC-100 beam and the NC-RAC-100 beam, the fractal dimensions of CCs of the former are mostly greater than those of the latter, as shown in Figure 19e. At the 40th day of accelerated corrosion, compared to the NC-RAC-100 beam, the fractal dimension of the C-RAC-100 beam increases by 10.08%.

The scale coefficient indicates the complexity of the distribution of cracks, and the greater the number of CCs and the longer the length of the CCs, the greater the complexity of the distribution of cracks [39]. As illustrated in Figure 20, with an increase in the C-RCA replacement ratio, the scale coefficient shows a trend of first increasing and then decreasing as well. As the corrosion time increases, the scale coefficient of the CCs on the tension side

of each beam gradually increases. Among all the beams, the scale coefficient of the CCs on the tension side of the NC-RAC-100 beam changes smoothly, while the growth rate of the scale coefficient of the CCs on the tension side of the C-RAC beams is relatively fast in the early stage and then slows down later. This also confirms that the CC continues to extend with the corrosion time, and the distribution of the CCs is becoming increasingly complex. What is more, the scale coefficients of the CCs on the tension side of the C-RAC beams are approximately greater than those of the NC-RAC-100 beam, which is consistent with the results of the total length of the CCs mentioned in Section 3.1. During the process of accelerated corrosion, the scale coefficients of the CCs of the C-RAC-100 beam are greater than those of the NC-RAC-100 beam. On the 40th day of accelerated corrosion, compared to the NC-RAC-100 beam, the scale coefficient of the C-RAC-100 beam increases by 95.25%.

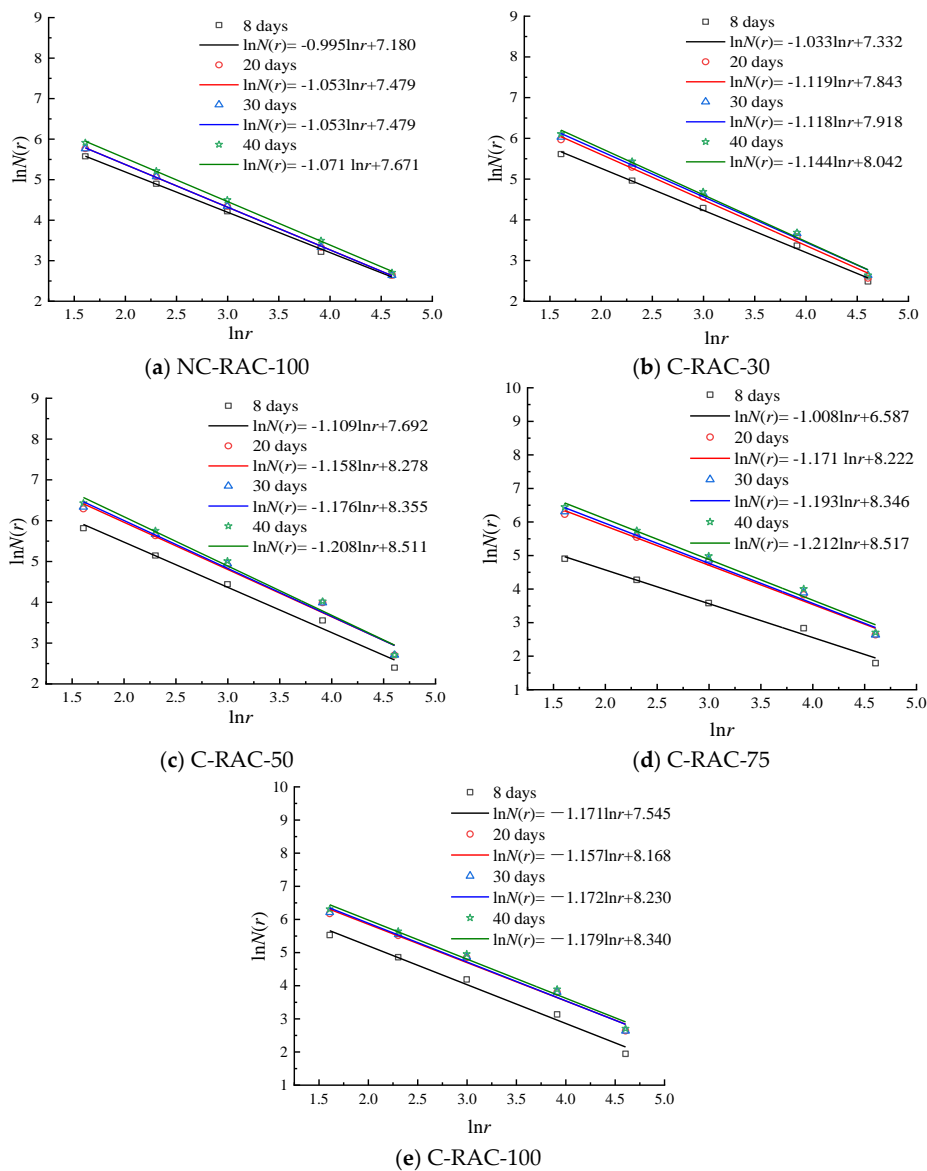


Figure 18. Fractal dimension and scale coefficient of CCs on the tension side of the beams.

Table 5. Computed results of the fractal dimension and the scale coefficient of CCs.

Beam ID	Parameter	NC-RAC-100	C-RAC-30	C-RAC-50	C-RAC-75	C-RAC-100
8 days	D	0.995	1.033	1.109	1.008	1.171
	C	1313	1528	2191	726	1891
	R^2	0.998	0.996	0.983	0.986	0.981
20 days	D	1.053	1.119	1.158	1.171	1.157
	C	1770	2548	3936	3722	3526
	R^2	0.999	0.992	0.976	0.984	0.982
30 days	D	1.053	1.118	1.176	1.193	1.172
	C	1770	2746	4251	4213	3752
	R^2	0.999	0.992	0.977	0.982	0.983
40 days	D	1.071	1.144	1.208	1.212	1.179
	C	2145	3109	4969	4999	4188
	R^2	0.999	0.992	0.977	0.980	0.982

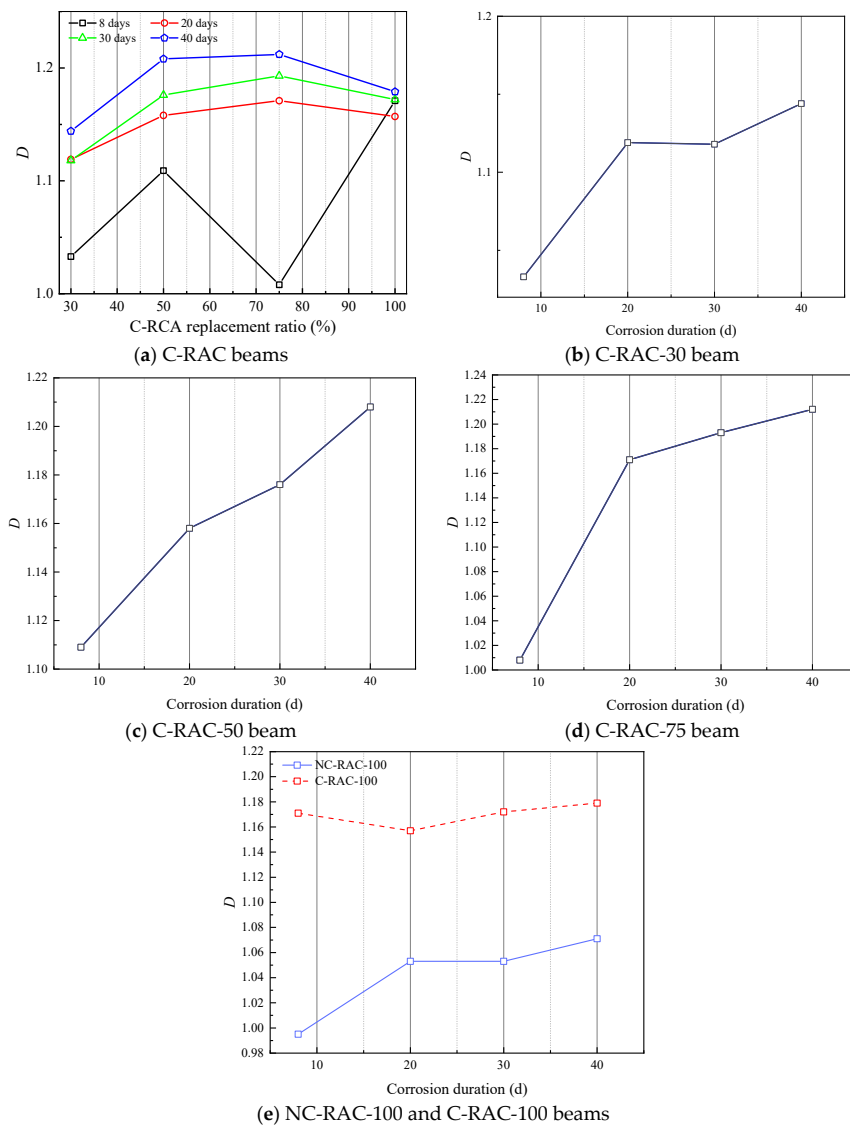


Figure 19. Comparison of the fractal dimensions of the CCs on the tension side of the beams.

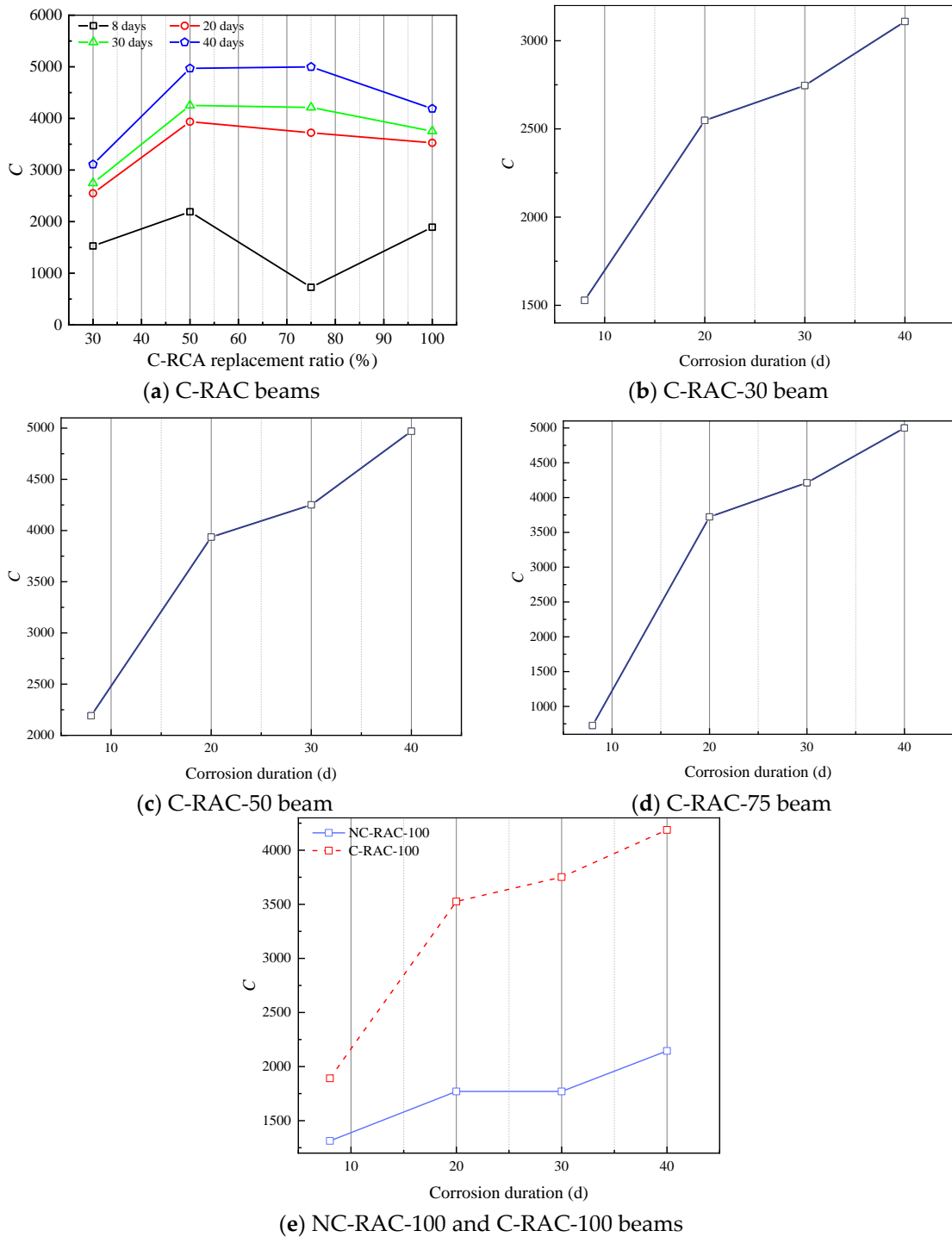


Figure 20. Comparison of the scale coefficients of the CCs on the tension side of the beams.

3.4. Deterministic Analysis of Corrosion Depth of Longitudinal Tensile Steel Bars in the C-RAC Beams

In order to compare the changes in the corrosion depth of longitudinal tensile steel bars along the length direction in different beams, the sum of the corrosion depths of two longitudinal tensile steel bars at the same position was calculated as the corrosion depth of longitudinal tensile steel bars at that position of the beam. The distribution of the corrosion depth of longitudinal tensile steel bars is shown in Figure 21. It can be observed from Figure 21 that the corrosion depth of longitudinal tensile steel bars along the length direction shows high randomness, illustrating that the corrosion of longitudinal tensile

steel bars is uneven. This is mainly due to the non-uniformity of C-RAC and the presence of CCs. As shown in Figure 21, the corrosion depth increases correspondingly with the mass loss of longitudinal tensile steel bars. With the increase in the C-RCA replacement ratio, the mass loss and the corrosion depth of longitudinal tensile steel bars in the beams both show a decreasing trend. Compared to the NC-RAC-100 beam, the mass loss of longitudinal tensile steel bars of the C-RAC-100 beam reduces by 37.91%, while the corrosion depth decreases by up to 85.46%. This is because after carbonation, the RCA becomes denser, and the bonding strengths among the coarse aggregates, old mortar, and the new cement paste are improved, which reduces the porosity and the micro-cracks of ITZs, and as a result, there are fewer defects (including micro-cracks and micro-pores) in the C-RAC than in the NC-RAC, which reduces the permeation channels of moisture, oxygen, and chloride ions inside C-RAC, thereby slowing down the corrosion rate of steel bars in the C-RAC-100 beam.

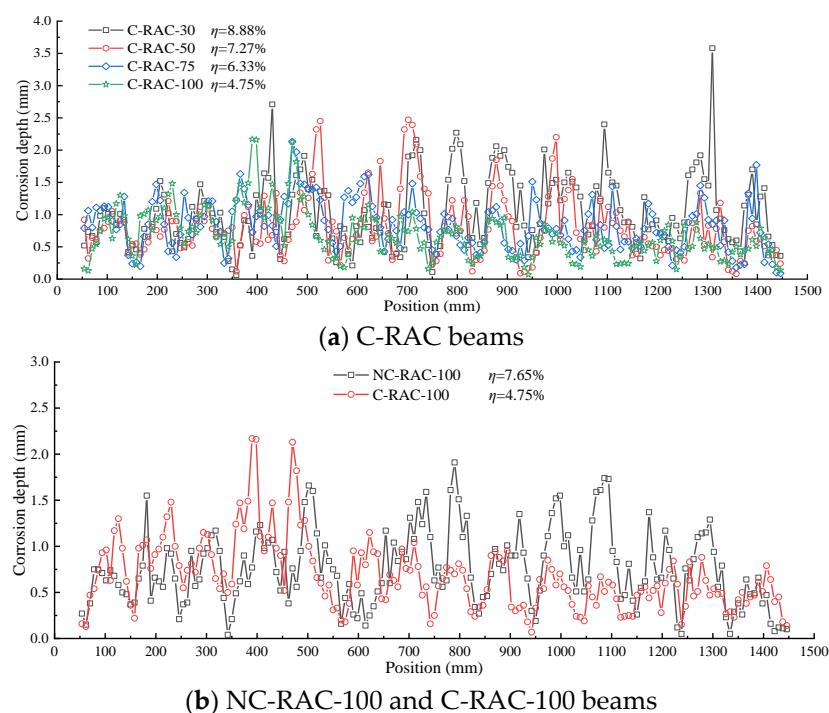


Figure 21. Distribution of the corrosion depth of longitudinal tensile steel bars along the length direction.

3.5. Probability Analysis of Corrosion Depth of Longitudinal Tensile Steel Bars in the C-RAC Beams

The durability of C-RAC beams is influenced by various factors such as the quality of the C-RCA, the mix proportions, and the internal unevenness. This leads to the corrosion process of steel bars being influenced by multiple factors, exhibiting high variability under different environmental conditions, which results in a certain degree of randomness and uncertainty in the corrosion depth of the longitudinal tensile steel bars. In this section, the probabilistic analysis method is also adopted to analyze the corrosion depth of the longitudinal tensile steel bars along the length direction. The frequency distribution histograms of the corrosion depth of longitudinal tensile steel bars in the beams are shown in Figure 22, and the curve fitting on the frequency distribution histograms are performed in the software Origin 2018. The best curve fitting is shown in Figure 22, and the fitted values of probability distribution parameters are tabulated in Table 6.

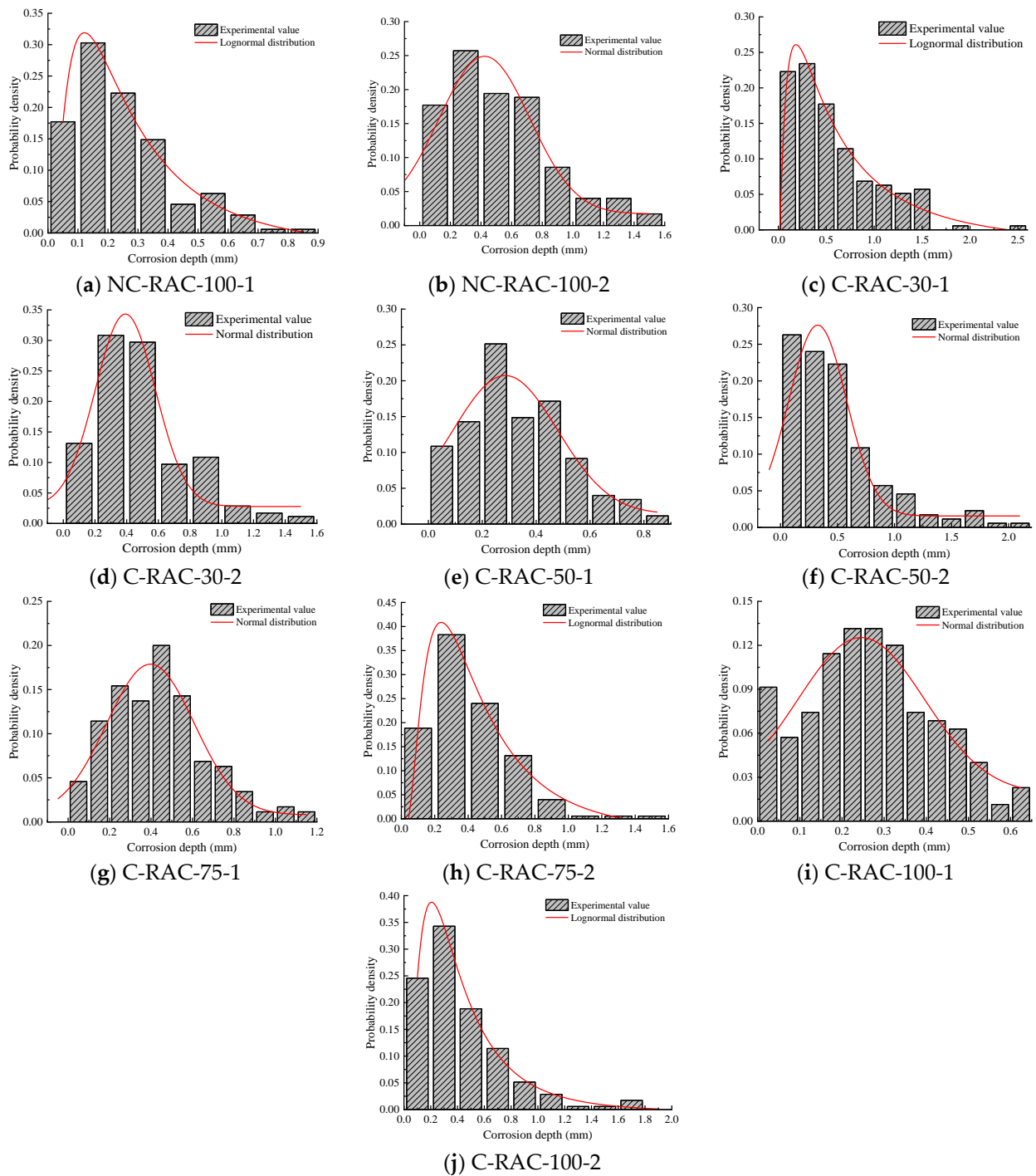


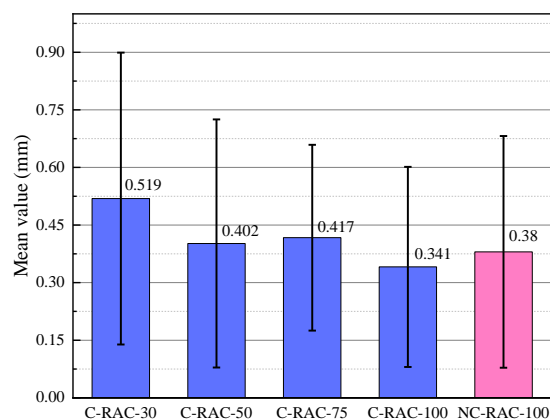
Figure 22. Frequency distribution histograms of the corrosion depth of the longitudinal tensile steel bars.

Table 6. Fitted values of probability distribution parameters of the corrosion depth.

Beam ID	Steel Bar	Mass Loss (%)	Distribution Function	y_0	x_c	w	A	R^2
NC-RAC-100	1	5.58	Lognormal	−0.024	0.251	0.852	0.127	0.967
	2	9.76	Normal	0.017	0.423	0.296	0.232	0.790
C-RAC-30	1	9.61	Lognormal	−0.021	0.662	1.132	0.279	0.973
	2	8.16	Normal	0.028	0.392	0.190	0.315	0.895
C-RAC-50	1	7.00	Normal	0.014	0.286	0.194	0.193	0.804
	2	7.54	Normal	0.016	0.326	0.253	0.260	0.824
C-RAC-75	1	5.81	Normal	0.008	0.397	0.211	0.171	0.891
	2	6.86	Lognormal	−0.027	0.406	0.729	0.247	0.988
C-RAC-100	1	3.41	Normal	0.018	0.246	0.150	0.107	0.783
	2	6.10	Lognormal	−0.004	0.366	0.760	0.205	0.995

As shown in Figure 22 and Table 6, the distribution of the corrosion depth of one longitudinal tensile steel bar in the NC-RAC-100 beam follows a normal distribution, while another one follows a lognormal distribution. For the C-RAC beams, the distribution of the corrosion depth of five longitudinal tensile steel bars follows a normal distribution, while another three follows a lognormal distribution, which indicates that the distribution of corrosion depth in the C-RAC beams is mainly a normal distribution. However, Wang et al. [42] found that the distribution of the corrosion depth of longitudinal tensile steel bars in NC-RAC beams under load is mainly a lognormal distribution, which is different from the results in this paper. The reason may be that the effect of load is not considered during the process of the accelerated corrosion test of the C-RAC beams in this paper.

The mean value and the C_v of the corrosion depth of the longitudinal tensile steel bars of each beam are calculated, as shown in Figures 23 and 24. Figure 23 shows that, with the increase in the C-RCA replacement ratio, the mean value of the corrosion depth of longitudinal tensile steel bars in the beams shows a decreasing trend. When the C-RCA replacement ratio increases from 30% to 100%, the mean value of the corrosion depth of longitudinal tensile steel bars decreases by 33.46%, while that of the C-RAC-100 beam reduces by 10.26% compared to that of the NC-RAC-100 beam.

**Figure 23.** Mean value of the corrosion depth.

The C_v of the corrosion depth of the longitudinal tensile steel bars represents the dispersion degree of corrosion depth around its mean value, as shown in Figure 24. Figure 24 indicates that there is no obvious difference in the C_v of the corrosion depth of longitudinal tensile steel bars of the two types of beams, and the values of C_v fluctuate between 0.58 and 0.81, showing a greater dispersion degree of the corrosion depth. The reason may be that although the fillers and protective layers generated during carbonation strengthening of RCA can delay the overall process of steel corrosion, its control over the discreteness of the corrosion process is limited. The C_v of the corrosion depth of the C-RAC-100 beam decreases by 3.77% compared to that of the NC-RAC-100 beam.

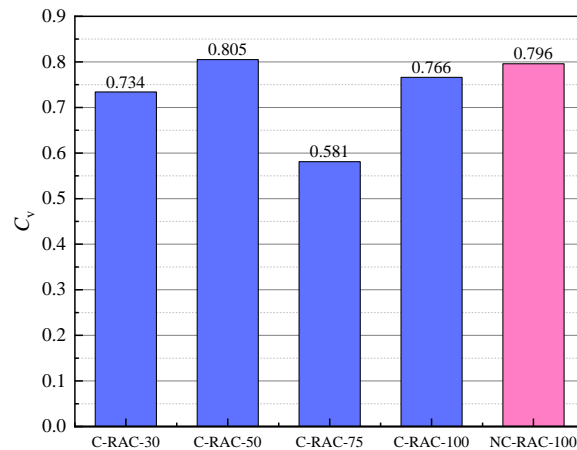


Figure 24. C_v of the corrosion depth.

The statistical distribution characteristics of the corrosion depth of the longitudinal tensile steel bars can be described by a box plot, as depicted in Figure 25. Figure 25 shows that when the C-RCA replacement ratio increases from 30% to 100%, the size of the box plot shows an approximately decreasing trend; that is, the corrosion depth tends to be concentrated, and the trend of the changes in quartiles and medians is basically the same as the trend of the changes in the mean value. It is evident that the statistical distribution characteristics of the corrosion depth are similar to those of the crack width as the C-RCA replacement ratio changes. Compared with the NC-RAC-100 beam, similar to the crack width distribution, the corrosion depth distribution of the C-RAC-100 beam is more concentrated, and the mean value, quartiles, and median are all reduced.

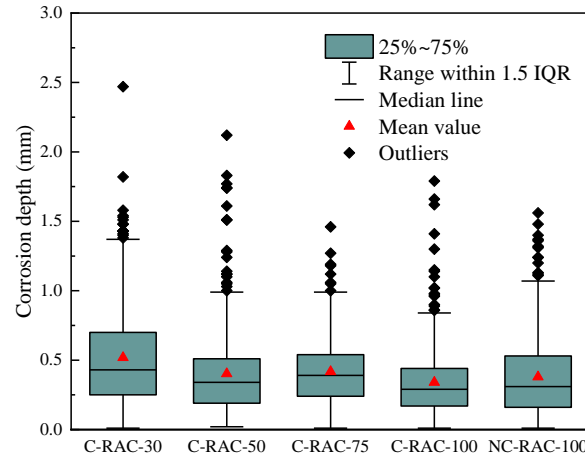


Figure 25. Box plot of the corrosion depth.

4. Conclusions

In this paper, the distribution and development laws of CCs and the corrosion depth characteristics of steel bars in C-RAC beams have been investigated through the accelerated corrosion test, and the main conclusions are as follows:

- (1) When accelerating corrosion for 40 days, compared to the NC-RAC-100 beam, the corrosion-induced cracking area of the C-RAC-100 beam decreases by 40.00%, while the total length of the CCs increases by 51.82%;
- (2) The type of probability distribution for the width of CCs on the tension side of the C-RAC beams is a lognormal distribution. As the C-RCA replacement ratio increases from 30% to 100%, the mean value of the width of CCs decreases by 54.17%, and the trend of changes in quartiles and medians is basically the same as the trend of changes in the mean value. Compared with the NC-RAC-100 beam, the mean value for the

width of CC of the C-RAC-100 beam decreases by 66.67%, the crack width distribution of the C-RAC-100 beam is more concentrated, and the quartiles and median are all reduced;

- (3) With an increase in the C-RCA replacement ratio, the fractal dimension and the scale coefficient of the CC on the tension side of the beams show an approximate trend of first increasing and then decreasing. When accelerating corrosion to the 40th day, compared to the NC-RAC-100 beam, the fractal dimension and scale coefficient of the C-RAC-100 beam increase by 10.08% and 95.25%, respectively;
- (4) With the increase in the C-RCA replacement ratio, the mass loss and the corrosion depth of longitudinal tensile steel bars in the beams both show a decreasing trend. Compared with the NC-RAC-100 beam, the mass loss of longitudinal tensile steel bars of the C-RAC-100 beam reduces by 37.91%, while the highest decrease in the corrosion depth is 85.46%;
- (5) The distribution of the corrosion depth of longitudinal tensile steel bars in the C-RAC beams is mainly a normal distribution. When the C-RCA replacement ratio increases from 30% to 100%, the mean value of the corrosion depth of longitudinal tensile steel bars decreases by 33.46%, and the trend of changes in quartiles and medians is basically the same as the trend of changes in the mean value. Compared with the NC-RAC-100 beam, the mean value of the corrosion depth of the C-RAC-100 beam reduces by 10.26%, the corrosion depth distribution is more concentrated, and the quartiles and median are all reduced;
- (6) In future research, it can be recommended to study the characteristics of corrosion-induced cracking and steel corrosion of carbonated recycled fine aggregate concrete beams and carbonated recycled fine and coarse aggregate concrete beams. In addition, more tests are needed to be designed to further study the characteristics of corrosion-induced cracking and steel corrosion of C-RAC beams, as well as the effect of the C-RCA replacement ratio on the fractal dimension and the scale coefficient of the CCs on the tension side of the C-RAC beams.

Author Contributions: P.G.: investigation, formal analysis, writing—original draft; J.W.: conceptualization, methodology, writing—review and editing, project administration, funding acquisition, supervision; B.C.: formal analysis, writing—original draft, writing—review and editing; M.B.: validation, writing—review and editing, project administration; Y.S.: data curation, writing—review and editing. All authors have read and agreed to the published version of the manuscript.

Funding: This research was funded by the project of experimental and numerical research on the strength, mix proportions, and durability of recycled concrete (No. HT-99982023-0558), which is sponsored by Beijing Tsingda Green Technology Co., Ltd.

Data Availability Statement: Data presented in this study can be made available on request from the corresponding author.

Conflicts of Interest: Author Pengfei Gao was employed by the company Inspection and Certification Co., Ltd. MCC, and author Mingxin Bai was employed by the company Shenzhen China Nuclear Power Engineering Design Co., Ltd. The remaining authors declare that the research was conducted in the absence of any commercial or financial relationships that could be construed as potential conflicts of interest. The funders had no role in the design of the study; in the collection, analyses, or interpretation of data; in the writing of the manuscript; or in the decision to publish the results.

References

1. Wang, J.; Su, H.; Du, J.S.; Yu, J. Corrosion-induced cracking of recycled aggregate concrete beams under static load. *Struct. Build.* **2023**, *176*, 800–814. [[CrossRef](#)]
2. Wang, J.; Qin, H.T.; Xu, Q. Flexural stiffness of recycled aggregate concrete beams under combined effect of load and steel corrosion. *Struct. Concr.* **2023**, *24*, 5909–5927. [[CrossRef](#)]
3. Zhang, H.R.; Zhao, Y.X. Integrated interface parameters of recycled aggregate concrete. *Constr. Build. Mater.* **2015**, *101*, 861–877. [[CrossRef](#)]

4. Ren, Q.; Pacheco, J.; Brito, J.D.; Hu, J. Analysis of the influence of the attached mortar's geometry on the mechanical behaviour of recycled aggregate concrete through mesoscale modelling. *Eng. Fract. Mech.* **2024**, *297*, 109876. [[CrossRef](#)]
5. Yang, W.; Hua, M.Q.; Zhu, P.H.; Liu, H.; Liu, S.F. Effect of adsorption mortar content on mechanical and chloride ion permeability properties of concrete. *Bull. Chinese Ceram. Soc.* **2020**, *39*, 1415–1420.
6. Tejas, S.; Pasla, D. Assessment of mechanical and durability properties of composite cement-based recycled aggregate concrete. *Constr. Build. Mater.* **2023**, *387*, 131620. [[CrossRef](#)]
7. Adessina, A.; Fraj, A.B.; Barthélémy, J.F. Improvement of the compressive strength of recycled aggregate concretes and relative effects on durability properties. *Constr. Build. Mater.* **2023**, *384*, 131447. [[CrossRef](#)]
8. Wang, Y.S.; Zheng, J.L.; You, F. Review on enhancement methods of recycled aggregate. *Mater. Rep.* **2021**, *35*, 05053–05061.
9. Guo, H.; Shi, C.J.; Guan, X.M.; Zhu, J.P.; Ding, Y.H.; Ling, T.C.; Zhang, H.B.; Wang, Y.L. Durability of recycled aggregate concrete—A review. *Cem. Concr. Compos.* **2018**, *89*, 251–259. [[CrossRef](#)]
10. Lu, Z.; Tan, Q.H.; Lin, J.L.; Wang, D.C. Properties investigation of recycled aggregates and concrete modified by accelerated carbonation through increased temperature. *Constr. Build. Mater.* **2022**, *341*, 127813. [[CrossRef](#)]
11. Liang, C.F.; Ma, H.W.; Pan, Y.Q.; Ma, Z.M.; Duan, Z.H.; He, Z.H. Chloride permeability and the caused steel corrosion in the concrete with carbonated recycled aggregate. *Constr. Build. Mater.* **2019**, *218*, 506–518. [[CrossRef](#)]
12. Shi, C.J.; Li, Y.K.; Zhang, J.K.; Li, W.G.; Chong, L.L.; Xie, Z.B. Performance enhancement of recycled concrete aggregate—A review. *J. Clean. Prod.* **2016**, *112*, 466–472. [[CrossRef](#)]
13. Liang, C.F.; Cai, Z.D.; Wu, H.X.; Xiao, J.Z.; Zhang, Y.M.; Ma, Z.M. Chloride transport and induced steel corrosion in recycled aggregate concrete: A review. *Constr. Build. Mater.* **2021**, *282*, 122547. [[CrossRef](#)]
14. Wang, J.Y. Effects of Recycled Concrete Aggregate Carbonated Treatments on Permeability and ITZs of Recycled Aggregate Concrete. Master's Thesis, Hunan University, Changsha, China, 2017.
15. Cao, Z.J. The Effect of Recycled Aggregate Treated by Carbon Dioxide on Properties of Recycled Concrete. Master's Thesis, Hunan University, Changsha, China, 2016.
16. Kou, S.C.; Zhan, B.J.; Poon, C.S. Use of a CO₂ curing step to improve the properties of a CO₂ prepared with recycled aggregates. *Cem. Concr. Compos.* **2014**, *45*, 22–28. [[CrossRef](#)]
17. Lin, G.H. The influences on Stress-Strain Curves of Recycled Concrete Enhanced by Recycled Aggregate Cured by CO₂. Master's Thesis, Fuzhou University, Fuzhou, China, 2017.
18. Wang, J.G. Delay Law and Improvement Mechanism of Durability of Recycled Concrete Under Complex Environmental Conditions. Ph.D. Thesis, Beijing University of Technology, Beijing, China, 2020.
19. Huang, K.L.; Xue, K.; Li, S.J. Research on salt corrosion resistance of recycled aggregate concrete after carbonation treatment. *Ind. Constr.* **2021**, *51*, 179–183.
20. Xuan, D.X.; Zhan, B.J.; Poon, C.S. Durability of recycled aggregate concrete prepared with carbonated recycled concrete aggregates. *Cem. Concr. Compos.* **2017**, *84*, 214–221. [[CrossRef](#)]
21. Liang, C.F.; Lu, N.; Ma, H.W.; Ma, Z.M.; Duan, Z.H. Carbonation behavior of recycled concrete with CO₂-curing recycled aggregate under various environments. *J. CO₂ Util.* **2020**, *39*, 101185. [[CrossRef](#)]
22. Zhan, B.J.; Xuan, D.X.; Zeng, W.L.; Poon, C.S. Carbonation treatment of recycled concrete aggregate: Effect on transport properties and steel corrosion of recycled aggregate concrete. *Cem. Concr. Compos.* **2019**, *104*, 103360. [[CrossRef](#)]
23. Zheng, J.L.; Hu, W.; Wang, Y.S. Influence of CO₂-enhancement recycled coarse aggregate on corrosion performance of rebar in concrete. *Eng. J. Wuhan. Univ.* **2020**, *53*, 225–231.
24. Liu, H.L. Research for Mechanical Performance of Reinforced RAC Large Eccentric Compressive Columns Under Load Coupled with Chloride Environment. Master's Thesis, Fuzhou University, Fuzhou, China, 2018.
25. Wang, J.; Su, H.; Du, J.S. Corrosion characteristics of steel bars embedded in recycled concrete beams under static loads. *J. Mater. Civil. Eng.* **2020**, *32*, 04020263. [[CrossRef](#)]
26. Wang, J.; Ng, P.L.; Qin, H.T.; Yuan, Y.Y. Recycled concrete beams subjected to combined reinforcement corrosion and static pre-loading. *Mag. Concr. Res.* **2023**, *75*, 703–722. [[CrossRef](#)]
27. Zou, Z.H.; Yang, G.J.; Su, T. Analytical model to predict residual flexural capacity of recycled aggregate concrete beams with corroded longitudinal rebars. *Adv. Mater. Sci. Eng.* **2020**, *3*, 1–11. [[CrossRef](#)]
28. Wang, J.; Xu, Q. The combined effect of load and corrosion on the flexural performance of recycled aggregate concrete beams. *Struct. Concr.* **2023**, *24*, 359–373. [[CrossRef](#)]
29. Peng, L.G.; Zhao, Y.X.; Zhang, H.R. Flexural behavior and durability properties of recycled aggregate concrete (RAC) beams subjected to long-term loading and chloride attacks. *Constr. Build. Mater.* **2021**, *277*, 122277. [[CrossRef](#)]
30. Zhang, H.R.; Zhao, Y.X. Performance of recycled concrete beams under sustained loads coupled with chloride ion (Cl⁻) ingress. *Constr. Build. Mater.* **2016**, *128*, 96–107. [[CrossRef](#)]
31. GB/T 25177; Recycled Coarse Aggregate for Concrete. General Administration of Quality Supervision, Inspection and Quarantine of China (AQSIQC): Beijing, China, 2010.
32. GB/T 50082; Standard for Test Methods of Long-Term Performance and Durability of Ordinary Concrete. General Administration of Quality Supervision, Inspection and Quarantine of China (AQSIQC): Beijing, China, 2009.
33. Wang, J.; Wang, Z.T.; Du, J.S. Corrosion characteristics of tapered sleeve locking-type splicing reinforcement in precast segmental bridge piers. *Structures* **2023**, *48*, 1907–1919. [[CrossRef](#)]

34. Yang, O.; Zhang, B.; Yan, G.R.; Chen, J. Bond performance between slightly corroded steel bar and concrete after exposure to high temperature. *J. Struct. Eng.* **2018**, *144*, 04018209. [[CrossRef](#)]
35. Coronelli, D.; Hanjari, K.Z.; Lundgren, K. Severely corroded RC with cover cracking. *J. Struct. Eng.* **2013**, *139*, 221–232. [[CrossRef](#)]
36. Zhao, Z.F.; Yao, L.; Xiao, J.Z.; Ji, C.Y.; Duan, Z.H.; Wang, D.C. Development on accelerated carbonation technology to enhance recycled aggregates. *J. Chin. Ceram. Soc.* **2022**, *50*, 2296–2304.
37. Wu, Z.W. Fracture Fractal and Bearing Capacity Evaluation of Small and Medium Span Concrete Beam Bridge. Master's Thesis, Chongqing Jiaotong University, Chongqing, China, 2020.
38. Zhou, J.H.; Wu, X.X.; Yu, H.L.; Zhao, Q.; Zhang, G.Q. Study on flexural performance of recycled concrete beams with waste fiber based on fractal theory. *J. Archit. Civ. Eng.* **2023**, *40*, 52–59.
39. Tong, J. Analysis on Entire Period of Corrosion-Induced Crack of Reinforced Concrete Based on Digital Image Correlation Method. Master's Thesis, Zhejiang University, Hangzhou, China, 2015.
40. Li, W.W.; Wu, M.Z.; Shi, T.S.; Yang, P.F.; Pan, Z.J.; Liu, W.; Liu, J.; Yang, X. Experimental investigation of the relationship between surface crack of concrete cover and corrosion degree of steel bar using fractal theory. *Fractal Fract.* **2022**, *6*, 325. [[CrossRef](#)]
41. Jiang, H.Y.; Jin, N.G.; Ye, H.L.; Tian, Y.; Jin, X.Y.; Zeng, Q.; Yan, D.M.; Xu, X. Fractal characterization of non-uniform corrosion of steel bars in concrete beams after accelerated depassivation and seven-year natural corrosion. *Materials.* **2019**, *12*, 3919. [[CrossRef](#)] [[PubMed](#)]
42. Wang, J.; Su, H.; Du, J.S. Corrosion depth of steel bars in recycled aggregate concrete beams under static load. *Struct. Build.* **2024**, *177*, 449–462. [[CrossRef](#)]

Disclaimer/Publisher's Note: The statements, opinions and data contained in all publications are solely those of the individual author(s) and contributor(s) and not of MDPI and/or the editor(s). MDPI and/or the editor(s) disclaim responsibility for any injury to people or property resulting from any ideas, methods, instructions or products referred to in the content.